

Coherent and Compact Zinc Electrodeposition Enabled by Compressing the Electric Double Layer of the Deposits

Ruirui Zhao

Tongji University

Haifeng Wang

Tongji University

Haoran Du

Tongji University

Ying Yang

Tongji University

Zhonghui Gao

Tianjin University

Long Qie (✉ qie@tongji.edu.cn)

Tongji University

Yunhui Huang

Huazhong University of Science and Technology <https://orcid.org/0000-0003-1687-1938>

Article

Keywords: electrodeposited Zn particles, van der Waals attraction, batteries

Posted Date: November 9th, 2021

DOI: <https://doi.org/10.21203/rs.3.rs-1024152/v1>

License: © ⓘ This work is licensed under a Creative Commons Attribution 4.0 International License.

[Read Full License](#)

Version of Record: A version of this preprint was published at Nature Communications on June 6th, 2022.
See the published version at <https://doi.org/10.1038/s41467-022-30939-8>.

Coherent and Compact Zinc Electrodeposition Enabled by Compressing the Electric Double Layer of the Deposits

Ruirui Zhao¹, Haifeng Wang¹, Haoran Du¹, Ying Yang¹, Zhonghui Gao¹, Long Qie^{1,2*}, and Yunhui Huang^{2*}

¹ Institute of New Energy for Vehicles, School of Materials Science and Engineering, Tongji University, Shanghai, 201804, China. ² State Key Laboratory of Material Processing and Die & Mold Technology, School of Materials Science and Engineering, Huazhong University of Science and Technology, Wuhan, Hubei Province, 430074, China.

*Corresponding author.

E-mail: qie@tongji.edu.cn; huangyh@hust.edu.cn

The porous hexagonal-platelet Zinc (Zn) deposits exacerbate the chemical corrosion and deteriorate the reversibility of the Zn electrodes in aqueous electrolytes. Based on the Derjaguin-Landau-Verwey-Overbeek (DLVO) theory, to turn the messy Zn deposits into agglomerate ones, the challenge is to weaken the electric double layer repulsive force, which is the main reason preventing the dense Zn deposits, between the electrodeposited Zn particles. Here, we proposed a strategy to compress the electric double layer and regulate the forces between the electrodeposited Zn particles by introducing inert charges to the surface of the Zn deposits. The results of the electron microscopies revealed dense and coherent electrodeposition of Zn, indicating that the van der Waals attraction between the deposits becomes governing during electrodeposition. Such results could be attributed to the adsorbed inert charges on Zn deposits decrease the net charges and weaken the electric double layer repulsive force. This design enables the Zn||Zn cells a long-term plating/stripping stability for > 1200 h, a high average Coulombic Efficiency of 99.9% for > 2100 h, and steady charge/discharge responses even under a draconian deep-discharge condition of 80% depth of discharge of Zn (DOD_{Zn}). In addition, the Zn||VS₂ full cells demonstrate significantly improved electrochemical reversibility and capacity retention.

Despite the advantages of aqueous Zn-based batteries (*e.g.*, Zn-MnO₂, Zn-Br₂, and Zn-Air batteries), including high safety, low cost, and nontoxicity, the sustained chemical corrosion and low reversibility of Zn electrodes encumber their practical applications. In aqueous electrolytes, the electrodeposition of hexagonal close-packed Zn metal has a strong propensity to form hexagonal platelets, which causes the deposited Zn a non-planar and flaky morphology¹⁻³. Such a porous structure is bound to exacerbate the chemical corrosion during the repeated plating and stripping of the Zn-metal phase due to the increased exposure of Zn electrodes to the electrolytes. The loose Zn flakes also cause the loss of electrical contact between the deposits and substrates and further deteriorates the reversibility of Zn electrodes⁴. What is worse, the dendritic Zn flakes may easily pierce the separator and lead to short circuits of batteries⁵.

To induce uniform Zn deposition with high reversibility, several strategies have been proposed: (1) constructing artificial interface layers to restrict the Zn crystal growth and isolate the Zn electrodes from aqueous electrolytes⁶⁻⁸; (2) using substrates with a low lattice mismatch and low affinity to lock the crystal orientation for the uniform Zn electrodeposition^{5, 9}; (3) increasing the driving force for the nucleation of Zn deposits to induce the uniform distribution of Zn-metal nuclei¹⁰. However, most of the above approaches rely on the modification of the Zn electrodes or current collectors, which decrease the overall energy density of the cells. Besides, the long-term cycling of Zn electrodes under conditions of high depth of discharge (DOD) and/or high areal capacity of Zn remains challenging. It is highly desired to explore new solutions to enable high effective Zn deposition without sacrificing the energy density.

The morphology of the deposited Zn directly affects the reversibility of Zn electrodes and the lifespan of Zn-based batteries¹¹⁻¹³. It is acknowledged that the morphology of the deposited Zn is related to multiple factors, including the intrinsic crystal anisotropy, electrolytes, substrate chemistry and geometry, and so on^{5, 10, 14-16}. The process of Zn

electrodeposition includes the desolvation and reduction of the Zn^{2+} ions, and the following formation and growth of the nucleus on conductive substrates. The final morphology of deposited metal is related to both the structure of as-formed grain crystals, which are always observed as irregular hexagonal flakes for Zn, and the interactions between them¹⁷. Based on the Derjaguin-Landau-Verwey-Overbeek (DLVO) theory, the interactions between Zn deposits in aqueous electrolytes are mainly related to the van der Waals (VDW) attractive force and the electrostatic repulsion due to the electric double layer (EDL) of counterions (**Figure S1** in Supporting Information)¹⁸⁻²⁰. In ZnSO_4 electrolyte, the electrodeposited Zn typically shows a loose and separate structure, indicating a repulsive-force-governed Zn deposition process. To induce dense and compact Zn coherent electrodeposition, we need to regulate the interactions between the Zn deposits from repulsion to attraction. As the VDW force, which depends mainly on the distance between the particles, could be considered as fixed for the Zn deposits, thus the solution is to weaken the EDL repulsion force between the Zn deposits.

Based on the Poisson-Boltzmann (PB) model, the EDL repulsive force between the negatively-charged surfaces of Zn deposits is mainly influenced by the thickness of the EDL, which is known as the Debye length ($1/\kappa$)¹⁷. Theoretically, by reducing the Debye length, the EDL repulsion force between two charged particles could be reduced. With this theory foundation, in this work, we introduced La^{3+} ions, which serve as high-valence competitive ions to decrease the Debye length²¹⁻²³, to the aqueous ZnSO_4 electrolytes. The electrochemical and morphology characterizations confirmed the presence of the insert La^{3+} ions weakens EDL repulsive force between the Zn deposits, changes the preferred orientation of Zn deposits, and results in dense and compact Zn coherent electrodeposition. With La^{3+} -modified electrolyte, the corrosion rate of Zn electrodes is significantly relieved with the corrosion current decreased from 421.6 to 6.3 $\mu\text{A cm}^{-2}$, enabling a high average Coulombic efficiency of > 99.9% for 2100 plating/stripping cycles. Even under an exacting condition with both a

high current density (10 mA cm^{-2}) and a limited Zn supply ($\text{DOD}_{\text{Zn}} = 80\%$), the Zn||Zn cell with the modified electrolyte exhibited a stable Zn deposition for $\sim 160 \text{ h}$, whereas the control cell failed to work. The as-proposed strategy demonstrates the importance of the thickness of EDL on the electrodeposition behaviors of Zn^{2+} ions and might also be applicable for other metal anodes.

Results

High reversibility and stability of Zn electrodes in ZSL electrolyte. The La^{3+} -modified electrolyte (ZSL) was prepared by dissolving $\text{La}(\text{NO}_3)_3$ into ZnSO_4 solution (ZS), the most widely-used electrolyte for aqueous Zn-ion batteries. To verify the effects of La^{3+} on Zn deposition, we firstly compared the plating/stripping performance of Zn||Zn cells in ZS and ZSL electrolytes with a current density of 1 mA cm^{-2} and an areal capacity of 1 mAh cm^{-2} (**Figure 1a**). The Zn||Zn cell with ZL electrolyte shows a decreasing voltage hysteresis (the voltage difference between the middle of the plating and stripping curves) during the first 50 h. However, the stabilized voltage drops suddenly after $\sim 320 \text{ h}$, indicating the failure of the cell. In comparison, the Zn||Zn cell with ZSL electrolyte exhibits stable voltage profiles $> 1200 \text{ h}$ with a negligible potential fluctuation. The voltage hysteresis remained $< 100 \text{ mV}$ during cycling. Such a stable long-term and steady voltage hysteresis illustrate the excellent stability of Zn electrodes in ZSL electrolyte. Similar results are also observed at a lower current density of 0.5 mA cm^{-2} , where the Zn||Zn cell with ZSL electrolyte survived $> 1800 \text{ h}$, much longer than the one in ZS electrolyte ($\sim 440 \text{ h}$, **Figure S2** in Supporting Information).

To figure out how the ZSL electrolyte affects the Zn electrodeposition, we disassembled the cycled Zn||Zn cells (100 cycles with a current density 1 mA cm^{-2} of and an areal capacity of 1 mAh cm^{-2}) and analyzed the morphology of the cycled Zn electrodes by a scanning electron microscopy (SEM). As the results shown in Figures 1b, the cycled Zn electrode in ZS electrolyte shows a highly porous surface that is stacked by thin Zn flakes with sharp edges,

which may pierce the separator and fail the cell⁵. In addition, the loose structure also leads to more side reactions between the Zn electrode and electrolyte due to the larger exposed surface, and thus more by-products accumulation. In comparison, after being cycled under a same test condition, the Zn electrode with ZSL electrolyte displays a dense surface with the deposited Zn flakes closely connected with each other (Figure 1c). Figure 1d displays the cross-sectional SEM image of the cycled Zn electrodes in ZS electrolyte, where the Zn electrode is almost depleted with only 12 μm in thickness of Zn foil left, indicating the formation of the large amounts of electrically-isolated “dead” Zn and by-products²⁴⁻²⁵. In contrast, the cycled Zn electrode in ZSL electrolyte shows a dense and thin Zn-deposition layer with $\sim 74 \mu\text{m}$ Zn foil left (Figure 1e). Considering the thickness of the fresh Zn electrode used is 80 μm , the use of ZSL electrolyte reduces the Zn consumption by 91% (from 68 μm to 6 μm in thickness) compared with the one in ZS electrolyte. The SEM results demonstrate that the introduction of $\text{La}(\text{NO}_3)_3$ into the ZS electrolyte induces dense Zn electrodeposition and enhances the utilization of Zn foil.

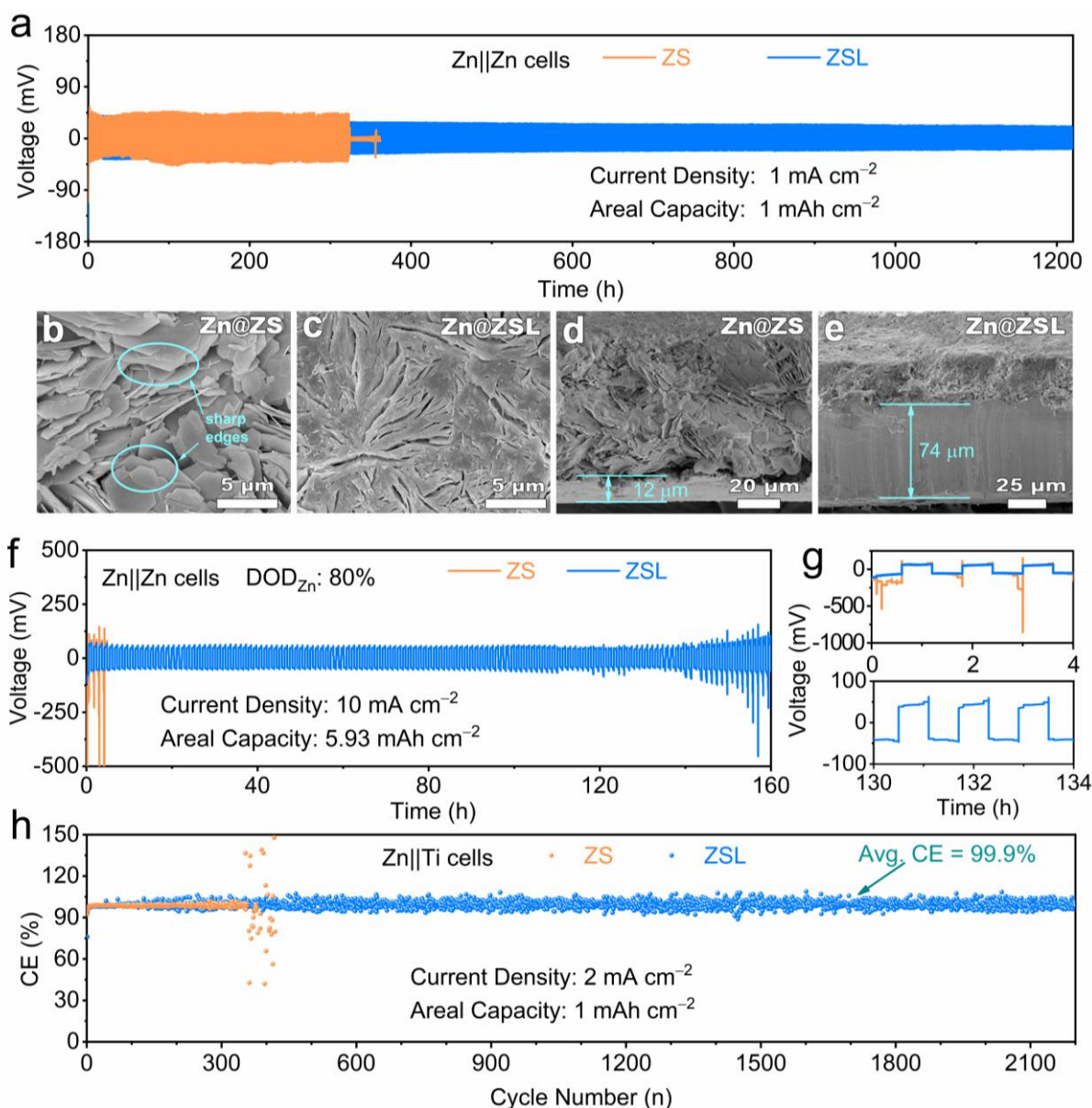


Figure 1 The plating/stripping behaviors for Zn electrodes in ZS and ZSL electrolytes: (a) cycling performance of the Zn||Zn cells with a current density of 1 mA cm^{-2} and an areal capacity of 1 mAh cm^{-2} ; the top and cross-sectional SEM images of the Zn electrodes in (b, d) ZS and (c, e) ZSL electrolytes after 100 cycles; (f) cycling performance of the Zn||Zn cells with a limited Zn supply ($\text{DOD}_{\text{Zn}} = 80\%$), a current density of 10 mA cm^{-2} , and an areal capacity of 5.93 mAh cm^{-2} ; (g) the selected enlarged voltage profiles of (f); (h) CE of the Zn||Ti cells with a current density of 2 mA cm^{-2} and a cut-off charging voltage of 0.4 V.

For practical applications, the depth of discharge of the Zn electrodes (DOD_{Zn}) significantly affects the cycling life and the overall energy density of the full cell⁴. The plating/stripping performance of the symmetrical Zn||Zn cells under different DOD_{Zn} was tested using thin Zn electrodes ($13 \text{ }\mu\text{m}$, 7.40 mAh cm^{-2}) with ZS and ZSL electrolyte. Figure

If displays the results of the cells under a rigorous condition of $\text{DOD}_{\text{Zn}} = 80\%$ (10 mA cm^{-2} , 5.93 mAh cm^{-2}). Under such a high DOD_{Zn} , the control Zn||Zn cell with ZS electrolyte showed a sharp voltage increase at the end of the initial stripping/plating process and died after struggling for only 3 h (Figure 1g). When ZSL electrolyte was employed, the cell exhibited stable voltage profiles $> 140 \text{ h}$ with a voltage hysteresis of $\sim 100 \text{ mV}$. Such extraordinary improvement in cycle life confirms the superiority of the ZSL electrolyte for practical high-capacity and deep-discharging conditions.

We further investigated the reversibility of Zn electrodes in ZS and ZSL electrolytes with Zn||Ti cells by plating 1 mAh cm^{-2} of Zn onto the Ti foil at a current density of 2 mA cm^{-2} and then stripping to 0.4 V . Figure 1h shows the Coulombic efficiency (CE) of both cells. The control cell with ZS electrolyte failed after only < 400 plating/stripping cycles with obvious fluctuation of the CE noticed at the end of cycle life, indicating the poor reversibility of Zn in ZS electrolyte. While when ZSL electrolyte was used, the cell delivered 2100 plating/stripping cycles with an average CE of 99.9%, surpassing most of the reported values²⁶⁻²⁷. Similar results are also obtained when the Ti-foil electrodes were replaced by carbon papers (**Figure S3** in Supporting Information). These results corroborate the introduction of $\text{La}(\text{NO}_3)_3$ additive into ZS electrolyte can effectively restrain the side reactions and improve the reversibility of Zn during long-term stripping/plating cycles.

The morphology analysis of Zn deposits. It is known that the Zn deposits in ZS electrolyte tend to exhibit a hexagonal-platelet morphology due to the lower thermodynamic free energy of the exposed (002) plane⁵. To investigate how the ZSL electrolyte affects the electrodeposition behavior of Zn, we checked the morphology for Zn deposits in ZS and ZSL electrolytes at different current densities with a fixed deposition amount of 1 mAh cm^{-2} . As the SEM images shown in **Figures 2a ~ d**, the Zn deposits obtained in ZS electrolyte are built with hexagonal platelets, and the thickness of the platelets increases gradually with the increase of the current densities. However, even when the current density was increased to 20

mA cm^{-2} , the as-deposited platelets remained scattered. Such loose and separate structures are resulted from the strong repulsion force between the Zn deposits, which prevents the consolidation of the platelets. Surprisingly, the Zn deposits show dense and compact morphologies in ZSL electrolyte at all the current densities from 1 to 20 mA cm^{-2} (Figures 2e ~ h). The high-magnification SEM image for Zn deposits at a current density of 1 mA cm^{-2} displays that the compact Zn deposits are piled with Zn platelets (Figure 2i), the disappearance of the gaps between the Zn platelets reveals that the interactions between the Zn deposits have been successfully regulated from repulsion to attraction by adding $\text{La}(\text{NO}_3)_3$ into the ZS electrolyte.

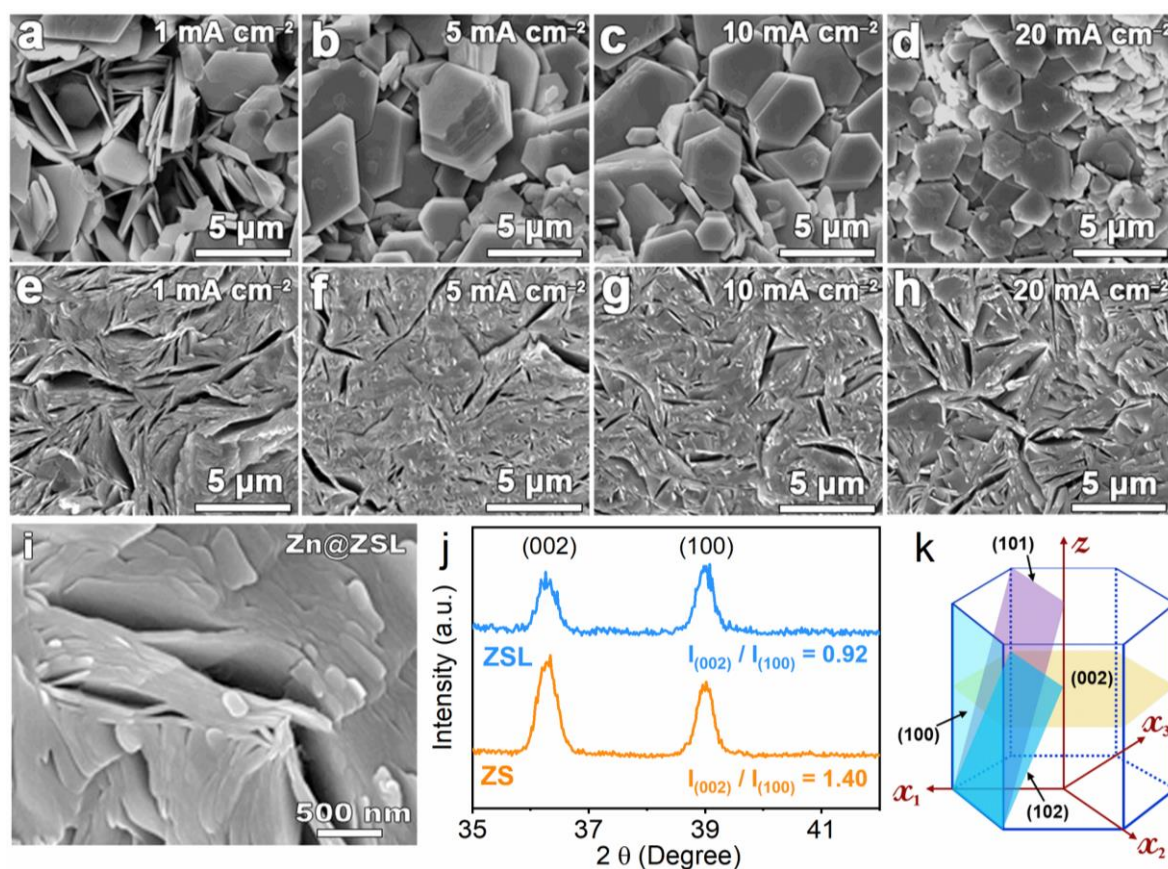


Figure 2 The SEM images of Zn deposits with a fixed areal capacity of 1 mAh cm^{-2} and different current densities from 1 to 20 mA cm^{-2} in (a ~ d) ZS and (e ~ h) ZSL electrolytes; (i) the high-magnification SEM image of the cycled Zn electrode in ZSL electrolyte; (j) GIXRD patterns of Zn deposits showing the reduced (002) planes in ZSL electrolyte; (k) the illustration of the hexagonal close packed (hcp) structure of Zn.

The structure of the Zn deposits obtained from ZS and ZSL electrolytes was further characterized by grazing incidence X-ray diffraction (GIXRD), a powerful tool to investigate the texturing and orientation anisotropy of thin film. As the results shown in Figure 2j, the Zn deposits obtained in ZSL electrolyte display a relatively weaker (002) peak. Quantitatively, the relative intensity ratio of peak (002) ($I_{(002)}$) to that of peak (100) ($I_{(100)}$) decreases from 1.4 to 0.92, indicating that the reduced (002) planes for the Zn deposits in ZSL electrolyte. Considering the hcp structure of Zn (Figure 2k) and reduced (002) plane of the Zn deposits obtained from ZSL electrolyte, it is safe to conclude that the as-obtained Zn deposits are piled up along the c axis, which could be regarded as a coherent deposition^{1, 28}.

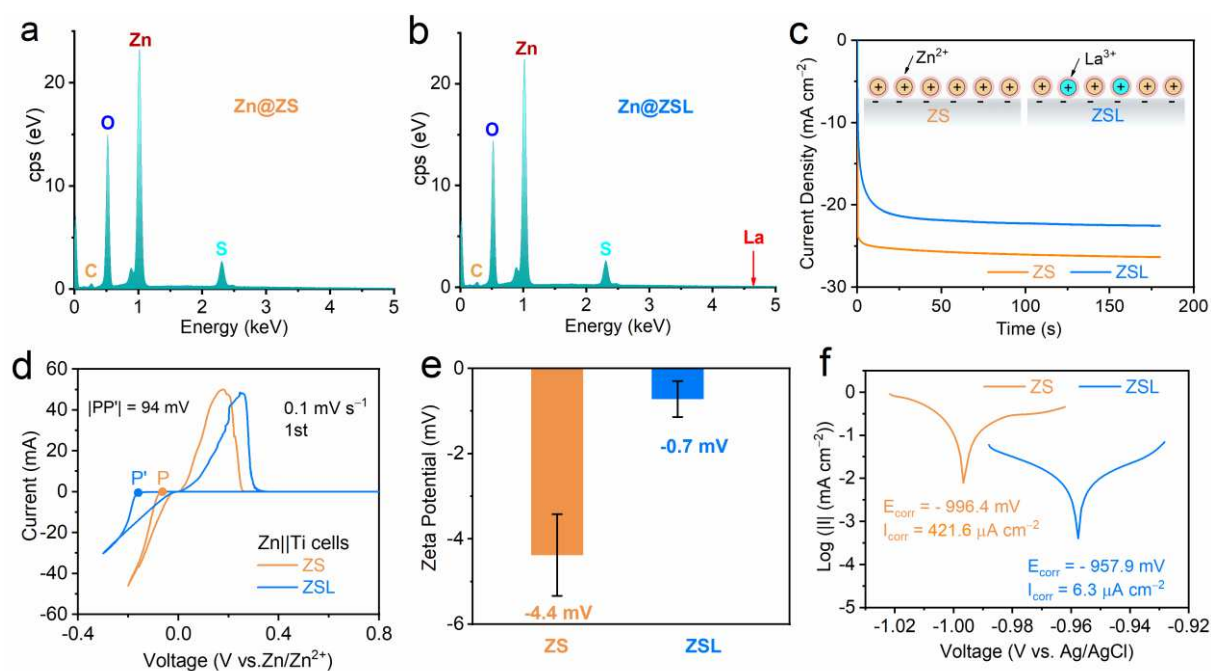


Figure 3 EDS of the Zn electrodes disassembled from the Zn||Zn cells after 100 cycles in (a) ZS and (b) ZSL electrolytes; (c) Chronoamperogram (CA) of the Zn electrodes in a three-electrode system with ZS or ZSL electrolytes at an overpotentials of -200 mV; (d) cyclic voltammograms (CV) of Zn||Ti cells in ZS and ZSL electrolytes; (e) the statistical Zeta potentials of Zn flakes in ZS and ZSL electrolytes; (f) linear polarization curves of the Zn electrodes collected with a scanning rate of 0.1 mV s^{-1} in ZS and ZSL electrolytes.

The role of net charges on the surface of Zn deposits in Zn deposition. To distinguish the function of $\text{La}(\text{NO}_3)_3$ additive, we prepared another control electrolyte (marked as ZSN),

which has the same NO_3^- concentration as that of the ZSN electrolyte (0.0255 m), by adding $\text{Zn}(\text{NO}_3)_2$ to the ZS electrolyte. The cycling stability of the $\text{Zn}||\text{Zn}$ cells with ZS, ZSL, and ZSN electrolytes was compared with a current density of 1 mA cm^{-2} and an areal capacity of 1 mAh cm^{-2} (**Figure S4** in Supporting Information). The cell with ZSN electrolyte dead after ~ 550 cycles, longer than the control cell, but only less than half of the one using ZSL electrolyte (> 1200 cycles). Such results imply that the improved cycling stability of the Zn electrodes in ZSL electrolyte is mainly attributed to the La^{3+} ions. To determine how the La^{3+} ions affect the Zn plating/stripping behaviors, we further investigated the cycled Zn electrodes in ZS and ZSL electrolytes with energy-dispersive X-ray spectroscopy (EDS). As the results shown in **Figures 3a** and **3b**, only the signals belonging to C, S, O, and Zn elements are detected for both samples. The absence of the La in the cycled Zn electrode with ZSL electrolyte suggests that the La^{3+} ions in ZSL electrolyte are not reduced or involved in the formation of the by-products. The inert nature of La^{3+} ions guarantees the durability of the ZSL electrolyte during long-term cycling.

The Zn deposits growth mechanism in ZS and ZSL electrolyte was further investigated by Chronoamperometry (CA), an electrochemical method to characterize the concentration change of electroactive species in the vicinity of the surface²⁹. The current response, which is determined by the nucleation centers³⁰⁻³², is recorded vs. time of the $\text{Zn}||\text{Zn}$ cells with ZS and ZSL electrolytes at an overpotential of -200 mV for a deposition time of 180 s is provided in **Figure 3c**. In ZS electrolyte, the current density reaches its steady value ($\sim -26 \text{ mA cm}^{-2}$) soon after the overpotential was applied, implying the immediate activation of all the nucleation sites and an instantaneous nucleation dominated process. In contrast, the current density for the cell with ZSL electrolyte is characterized by prolonged activation time, indicating that the number of nuclei increases gradually with time and the progressive nucleation is governing during Zn deposition in ZSL electrolyte^{29, 31}. It is also noticed that the steady current density in ZS electrolyte ($\sim -26 \text{ mA cm}^{-2}$) is higher than that in ZSL

electrolyte ($\sim -22 \text{ mA cm}^{-2}$). The differences in the nucleation mechanisms and steady current densities could be ascribed to the absorption of the inert La^{3+} ions on the surface of the Zn electrodes, which decrease the number of the active nucleation sites and slow down the formation of the nuclei in ZSL electrolyte.

The absorption of metal ions on an electrode is typically regarded as a monolayer-adsorption process³³. According to the Langmuir isotherm, the relationship between the equilibrium coverage (θ) and the concentration (c) of the adsorbents in the bulk solution follows equation (1):

$$\theta = \frac{cK}{1 + cK} \quad (1)$$

Where K is the equilibrium constant and depends only on the electrode potential and temperature. As the concentration of $\text{La}(\text{NO}_3)_3$ in ZSL electrolyte is only 0.0085 m, much less than that of ZnSO_4 (2 m), the equilibrium adsorbent coverage θ could be regarded as the same for the Zn electrodes in ZS and ZSL electrolytes, which means the current density (j) of the CA curves is proportional to the number of the adsorbed Zn^{2+} ions. In other words, the lower current density signifies less Zn^{2+} ions are adsorbed on the electrode in ZSL electrolyte, which is the result of the complete adsorption of inert La^{3+} ions. Besides, the Zn nucleation in ZSL electrolyte shows larger polarization voltage than that in ZS electrolyte ($|\text{PP}'| = 94 \text{ mV}$, Figure 3d), also reflecting the competitive adsorption between Zn^{2+} and La^{3+} ions in ZSL electrolyte.

To analyze the net charge of the Zn deposits in ZS and ZSL electrolytes, we collected the electrodeposited Zn flakes from the plated Ti-foil electrodes and checked their Zeta potentials. As the results shown in Figure 3e, the deposited Zn flakes obtained from ZS electrolyte show a Zeta potential of $\sim -4.4 \text{ mV}$, indicating that the Zn deposits are negatively charged. These negatively charged Zn flakes repel with each other, leading to the loose and separate Zn deposits in ZS electrolyte. In comparison, a Zeta potential of the Zn deposits obtained from ZSL electrolyte is only $\sim -0.7 \text{ mV}$, implying fewer net charges on the surface of Zn flakes

and compressed EDL. Fewer net charges on the surface of Zn deposits lead to a reduced EDL force between Zn deposits. Based on the DLVO theory, the interaction between the Zn deposits is determined by the EDL repulsion and the VDW attraction (Figure S1)¹⁹. With the reduced EDL force between Zn deposits in ZSL electrolyte, the VDW attraction becomes prominent, and the deposited Zn flakes tend to agglomerate along the (002) plane (**Figure S5**), leading to the formation of the dense and stacked Zn deposits.

The introduction of La³⁺ into ZS electrolyte also suppresses the parasitic reaction between electrolytes and Zn electrodes. As the linear polarization curves of the Zn electrodes in ZS and ZSL electrolytes shown in Figure 3f. Compared with that of the Zn electrodes in ZS electrolyte, the corrosion potential of the Zn electrode in ZSL electrolyte increases from -996.4 to -957.8 mV, implying a lower tendency of corrosion of Zn electrodes. In addition, the corrosion current (I_{corr}) of Zn electrodes is reduced from 421.6 $\mu\text{A cm}^{-2}$ in ZS electrolyte to 6.3 $\mu\text{A cm}^{-2}$ in ZSL electrolyte, implying that the corrosion was inhibited by 98% with the addition of La³⁺ based on the equation (2)³⁴.

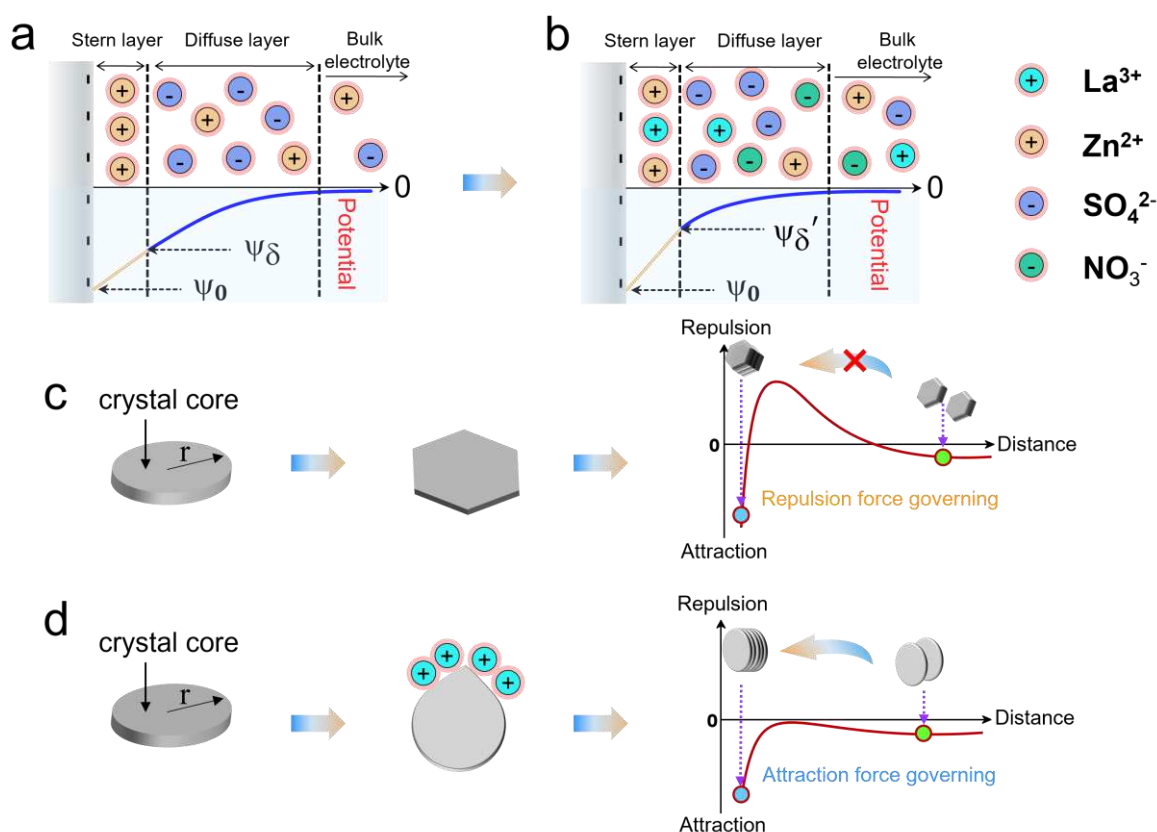


Figure 4 The illustrations of the coherent electrodeposition induced by a compressed electric double layer of Zn flakes: the comparison of the electric double layer of the Zn deposits in (a) ZS and (b) ZSL electrolytes; the as-proposed growth models of the Zn deposits in (c) ZS and (d) ZSL electrolytes.

Based on the above discussion, we illustrate the schemes of Zn coherent electrodeposition induced by compressed the electric double layer of Zn deposits. As shown in **Figures 4a** and **4b**, the Zn electrode is negatively charged during electrodeposition, delivering a potential of ψ_0 . According to the electric double layer theory, positive Zn^{2+} ions are absorbed onto the Zn electrode. Thereby, the potential of the surface of Zn deposits in ZS electrolyte increases from ψ_0 to ψ_δ . While in ZSL electrolyte, both the bivalent Zn^{2+} ions and trivalent La^{3+} ions are absorbed on the surface of Zn deposits, resulting in fewer net negative charges than that in ZS electrolyte. In this context, the surface of Zn deposits presents a higher potential ψ_δ' than ψ_δ . The EDL repulsion decreases due to the fewer net charges, and the Stern layer gets thinner in a ZSL electrolyte than in a ZS electrolyte³⁵. As illustrated in **Figure 4c**, in ZS electrolyte, the electrodeposited Zn tends to grow into separate hexagonal plates due

to the EDL repulsion dominated interactions between the Zn deposits³⁶. While when ZSL electrolyte is used, the competitive absorption of the inert La^{3+} ions on the surface of the Zn electrodes reduces the EDL repulsion between the Zn deposits and leads to the coherent electrodeposition of the Zn deposits along (002) plane (Figure 4d).

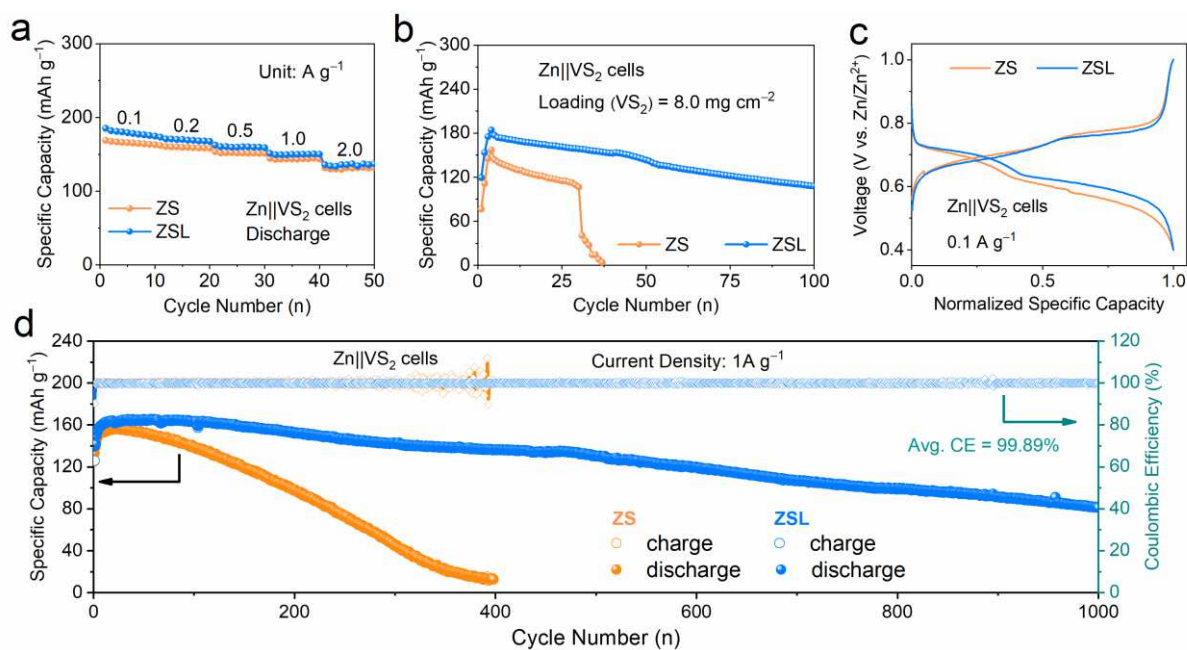


Figure 5 The electrochemical performance of Zn||VS₂ cells in ZS and ZSL electrolytes: (a) the rate performance; (b) the cycling performance with a limited Zn supply (N/P capacity ratio: 4.3); (c) normalized charge-discharge curves of (b) at the 20th cycle; (d) the cycling performance at a current density of 1.0 A g⁻¹.

The superior electrochemical performance of Zn||VS₂ cells with ZSL electrolyte.

The superiority of the ZSL electrolyte was also demonstrated in full cells with VS₂ cathodes (Figure 5). Here, the flower-like VS₂ was synthesized via a hydrothermal method (Figures S6 and S7 in Supporting Information). The Zn||VS₂ cell with ZSL electrolyte exhibits slightly higher specific capacities than those with ZS electrolyte at current densities of 0.1, 0.2, 0.5, 1.0, and 2.0 A g⁻¹ (Figure 5a). We further tested the cycling performance of the Zn||VS₂ cell with a limited Zn supply (7.4 mAh cm⁻²) and a high-loading VS₂ cathode (8.0 mg cm⁻²) at a current density of 0.1 A g⁻¹ after 5 activation cycles at 0.05 A g⁻¹. As the results displayed in Figure 5b, the Zn||VS₂ cell with ZS electrolyte shows a rapid capacity decay and dead after 30 cycles. Whereas, the cell with ZSL electrolyte remains a discharge capacity of 108 mA g⁻¹

after 100 cycles. The normalized discharge/charge profiles of the Zn||VS₂ cell at the 20th cycle were compared in Figure 5c, where the cell in ZS electrolyte shows larger voltage hysteresis (the voltage gap at 50% capacity) than that of the one in ZSL electrolyte. In addition, the voltage hysteresis of the cells in ZSL electrolyte decreases slightly from 118 mV in the 6th cycle to 101 mV in the 24th cycle, whereas the ones in ZS electrolyte increases gradually with cycles (Figure 5c and **Figure S8**), which may be explained by the improved stability and reduced by-products formation of Zn anode in ZSL electrolyte. The long-term cycling stability of Zn||VS₂ cells in ZS and ZSL electrolytes at a current density of 1 A g⁻¹ are compared in Figure 5d. Benefitting from the improved stability and reversibility of the Zn electrode in ZSL electrolyte, the Zn||VS₂ cell with ZSL electrolyte delivers superior cycling stability (1000 cycles) with a high average CE of 99.89%. In comparison, the Zn||VS₂ cell with ZS electrolyte faded quickly and dead in < 400 cycles. This superior electrochemical reversibility and capacity retention of Zn||VS₂ full-cells prove that regulation of interaction forces between Zn deposits is practical to promote the applications of aqueous Zn-based batteries.

Discussion

In summary, by introducing high-valence La³⁺ ions into the most popular aqueous ZnSO₄ electrolyte, we successfully compressed the EDL, reduced the EDL repulsion between the Zn deposits, and obtained coherent-electrodeposited Zinc with a compact structure and significantly improved electrochemical stability. With this EDL-compressing approach, a stable Zn plating/stripping performance for > 1200 h, a high average Coulombic efficiency of 99.9% for over 2100 cycles, a prolonged cycling stability under a draconian deep-discharge condition (80% DOD_{Zn}), and superb full-cell performance were realized. This work provides a new insight into the electrodeposition of Zn and paves the way to the practical applications of aqueous Zn-based batteries.

Methods

The preparation of the electrolytes. The ZS electrolyte (2m ZnSO₄) was prepared by dissolving 17.25 g of ZnSO₄ (99.995%, Aladdin) into 30 ml of deionized (DI) water. The ZSL electrolyte (2m ZnSO₄ and 0.0085m La(NO₃)₃) was prepared by adding 110.4 mg of La(NO₃)₃ (99%, Aladdin) into 30 mL of ZS solution. Here, the optimal concentration of La³⁺ ions was obtained by comparing the plating/stripping performance of Zn||Zn cells in the electrolytes with different La³⁺ concentrations. To inquire the role of NO₃⁻, ZSN electrolyte with a same concentration of NO₃⁻ as ZSL was prepared by adding 113.8 mg of Zn(NO₃)₂ (AR, Sinopharm Chemical) into 30 mL of ZS solution.

Synthesis of VS₂ powders. VS₂ Powders were synthesized by a previously-reported hydrothermal method³⁷. In a typical procedure, 3 ml of NH₃·H₂O and 23 mmol of thioacetamide (TAA) was added to a 45 ml of 3 mmol NH₄·VO₃ solution one by one with an interval time of 1 h under stirring. After being stirred for another hour, the as-received brown mixture was transferred into a 50 ml Teflon-lined autoclave and maintained at 180 °C for 20 h. After the reaction, the solid product was collected by centrifuging and washing with DI water and ethanol thoroughly and dried in a vacuum oven at 50 °C overnight. Finally, the as-collected black powders were annealed in N₂ at 180 °C for 8 h to obtain the VS₂ powders.

Characterizations. The morphologies and structures of the samples were characterized by field emission scanning electron microscopy (SEM, Nova NanoSEM 450) equipped with energy-dispersive X-ray spectroscopy (EDS). X-ray diffraction (XRD) patterns were recorded with a Bruker-AXS microdiffractometer (D-8 ADVANCE) using Cu-K_{α1} radiation ($\lambda = 1.5406 \text{ \AA}$) from 10° to 90°. Grazing incidence X-ray diffraction (GIXRD) patterns were collected from 35 ~ 47° on a Rigaku SmartLab X-ray diffractometer with a Cu-K_{α1} radiation with a step size of 0.0001°.

Electrochemical measurements. The VS₂ electrodes were prepared by a blade-cast method. Briefly, the VS₂ powders, acetylene black carbon, and polyvinylidene fluoride (PVDF) were mixed with a weight ratio of 7 : 2 : 1 in n-methyl-2-pyrrolidone (NMP) with an electric mixer (AR-100, THINKY). Then, the as-prepared slurry was blade-casted onto a Ti foil (15 μm in thickness). After being dried in a vacuum oven at 50 °C overnight, VS₂ electrodes were obtained by cutting the above Ti foil into circular sheets with a

diameter of 8 mm. The CR-2032 coin cells were assembled using glass fiber (GF-B, $\Phi 19$) as separators, Zn plates or VS₂ electrodes as the working electrodes, and Zn plates, Ti foils, or carbon papers as the counter electrodes, 100 μ l of electrolytes were added to each cells. For the electrochemical characterizations of the Zn||VS₂ cells with a limited Zn supply (13 μ m, 7.40 mAh cm⁻²), the areal mass loading of VS₂ electrodes was \sim 8.0 mg cm⁻², while the number is \sim 1.0 mg cm⁻² for all other Zn||VS₂ cells. The CE tests was measured with Zn||Ti (or Zn||C) cells with a Zn deposition of 1.0 mAh cm⁻² (2 mA cm⁻² for 0.5 h) and a charge cut-off voltage of 0.4 V. All the above tests were performed on a Neware Battery Tester. To test the corrosion rate of Zn foil, a three-electrode cell was constructed using Zn foil as working electrode, Pt wire as counter electrode, and Ag/AgCl electrode as reference electrode and tested on an electrochemical workstation (VMP3, Bio-Logic). The efficiency of protection ($\eta\%$) for Zn electrodes in a ZSL electrolyte was calculated by using the values of the corrosion current I_{corr} showing as the equation 2:

$$\eta\% = \left(\frac{I_{\text{corr}}(\text{ZS}) - I_{\text{corr}}(\text{ZSL})}{I_{\text{corr}}(\text{ZS})} \right) \times 100 \quad (2)$$

The linear polarization curve, chronoamperometry (CA) (at overpotentials of -200 mV), and cyclic voltammetry (CV) curves at a scan rate of 0.1 mV s⁻¹ were recorded electrochemical workstation (VMP3, Bio-Logic). The Zeta potential was collected on a Zeta potential analyzer (Malvern Zetasizer Nano ZS90).

Data availability

All data that support the findings of this study are available from the corresponding author on reasonable request.

Reference

1. Sato, R. Crystal growth of electrodeposited zinc: an electron diffraction and electron microscopic study. *J. Electrochem. Soc.* **106**, 206-211, (1959).
2. Ma, L., Schroeder, M. A., Pollard, T. P., Borodin, O., Ding, M. S., Sun, R., Cao, L., Ho, J., Baker, D. R., Wang, C. & Xu, K. Critical factors dictating reversibility of the zinc metal anode. *Energy Environ. Mater.* **3**, 516-521, (2020).
3. Li, C., Xie, X., Liang, S. & Zhou, J. Issues and future perspective on zinc metal anode for rechargeable aqueous zinc-ion batteries. *Energy Environ. Mater.* **3**, 146-159, (2020).
4. Ma, L., Schroeder, M. A., Borodin, O., Pollard, T. P., Ding, M. S., Wang, C. & Xu, K. Realizing high zinc reversibility in rechargeable batteries. *Nat. Energy* **5**, 743-749, (2020).
5. Zheng, J., Zhao, Q., Tang, T., Yin, J., D. Quilty, C., D. Renderos, G., Liu, X., Deng, Y., Wang, L., C. Bock, D., Jaye, C., Zhang, D., S. Takeuchi, E., J. Takeuchi, K., C. Marschilok, A. & Archer, L. A. Reversible epitaxial electrodeposition of metals in battery anodes. *Science* **366**, 645-658, (2019).
6. Zhao, R., Yang, Y., Liu, G., Zhu, R., Huang, J., Chen, Z., Gao, Z., Chen, X. & Qie, L. Redirected Zn electrodeposition by an anti-corrosion elastic constraint for highly reversible Zn anodes. *adv. Funct. Mater.* **31**, 2001867, (2021).

7. Kang, L., Cui, M., Jiang, F., Gao, Y., Luo, H., Liu, J., Liang, W. & Zhi, C. Nanoporous CaCO₃ coatings enabled uniform Zn stripping/plating for long-life zinc rechargeable aqueous batteries. *Adv. Energy Mater.* **8**, 1801090, (2018).
8. Xie, X., Liang, S., Gao, J., Guo, S., Guo, J., Wang, C., Xu, G., Wu, X., Chen, G. & Zhou, J. Manipulating the ion-transference kinetics and interface stability for high-performance zinc metal anode. *Energy Environ. Sci.* **13**, 503-510, (2020).
9. Zhang, Q., Luan, J., Huang, X., Wang, Q., Sun, D., Tang, Y., Ji, X. & Wang, H. Revealing the role of crystal orientation of protective layers for stable zinc anode. *Nat. Commun.* **11**, 3961, (2020).
10. Zheng, J., Bock, D. C., Tang, T., Zhao, Q., Yin, J., Tallman, K. R., Wheeler, G., Liu, X., Deng, Y., Jin, S., Marschilok, A. C., Takeuchi, E. S., Takeuchi, K. J. & Archer, L. A. Regulating electrodeposition morphology in high-capacity aluminium and zinc battery anodes using interfacial metal-substrate bonding. *Nat. Energy* **6**, 398-406, (2021).
11. Cao, J., Zhang, D., Gu, C., Wang, X., Wang, S., Zhang, X., Qin, J. & Wu, Z. S. Manipulating crystallographic orientation of zinc deposition for dendrite-free zinc ion batteries. *Adv. Energy Mater.* **11**, 2101299, (2021).
12. Jin, S., Zhang, D., Sharma, A., Zhao, Q., Shao, Y., Chen, P., Zheng, J., Yin, J., Deng, Y., Biswal, P. & Archer, L. A. Stabilizing zinc electrodeposition in a battery anode by controlling crystal growth. *Small* **17**, 2101798, (2021).
13. Dong, Y., Zhang, Z., Alvarez, A. & Chen, I. W. Potential jumps at transport bottlenecks cause instability of nominally ionic solid electrolytes in electrochemical cells. *Acta Mater.* **199**, 264-277, (2020).
14. Zheng, J., Yin, J., Zhang, D., Li, G., Bock, D. C., Tang, T., Zhao, Q., Liu, X., Warren, A., Deng, Y., Jin, S., Marschilok, A. C., Takeuchi, E. S., Takeuchi, K. J., Rahn, C. D. & Archer, L. A. Spontaneous and field-induced crystallographic reorientation of metal electrodeposits at battery anodes. *Sci. Adv.* **6**, eabb1122, (2020).
15. Shi, F., Pei, A., Vailionis, A., Xie, J., Liu, B., Zhao, J., Gong, Y. & Cui, Y. Strong texturing of lithium metal in batteries. *Proc. Natl. Acad. Sci. U. S. A.* **114**, 12138-12143, (2017).
16. Monroe, C. & Newman, J. The impact of elastic deformation on deposition kinetics at lithium/polymer interfaces. *J. Electrochem. Soc.* **152**, A396, (2005).
17. Israelachvili, J. N. *Intermolecular and surface forces*, (Harcourt Brace & Company, **1991**).
18. Smith, A. M., Borkovec, M. & Trefalt, G. Forces between solid surfaces in aqueous electrolyte solutions. *Adv. Colloid Interface Sci.* **275**, 102078, (2020).
19. Christenson, H. K. DLVO (Derjaguin–Landau–Verwey–Overbeek) theory and solvation forces between mica surfaces in polar and hydrogen-bonding liquids. *J. Chem. Soc., Faraday Trans. 1* **80**, 1933-1946, (1984).
20. Lee, S.-Y., Lee, S.-H. & Park, J.-G. Interaction forces between silica particles and wafer surfaces during chemical mechanical planarization of copper. *J. Electrochem. Soc.* **150**, G327, (2003).
21. van Oss, C. J. & Giese, R. F. Surface modification of clays and related materials. *J. Dispersion Sci. Technol.* **24**, 363-376, (2007).
22. Omija, K., Hakim, A., Masuda, K., Yamaguchi, A. & Kobayashi, M. Effect of counter ion valence and pH on the aggregation and charging of oxidized carbon nanohorn (CNHox) in aqueous solution. *Colloids Surf., A* **619**, 126552, (2021).
23. Valmacco, V., Elzbiaciak-Wodka, M., Herman, D., Trefalt, G., Maroni, P. & Borkovec, M. Forces between silica particles in the presence of multivalent cations. *J. Colloid Interface Sci.* **472**, 108-115, (2016).
24. Fang, C., Li, J., Zhang, M., Zhang, Y., Yang, F., Lee, J. Z., Lee, M.-H., Alvarado, J., Schroeder, M. A., Yang, Y., Lu, B., Williams, N., Ceja, M., Yang, L., Cai, M., Gu, J., Xu, K., Wang, X. & Meng, Y. S. Quantifying inactive lithium in lithium metal batteries. *Nature* **572**, 511-515, (2019).
25. Huang, C.-J., Thirumalraj, B., Tao, H.-C., Shitaw, K. N., Sutiono, H., Hagos, T. T., Beyene, T. T., Kuo, L.-M., Wang, C.-C., Wu, S.-H., Su, W.-N. & Hwang, B. J. Decoupling the origins of irreversible coulombic efficiency in anode-free lithium metal batteries. *Nat. Commun.* **12**, 1452, (2021).
26. Sun, P., Ma, L., Zhou, W., Qiu, M., Wang, Z., Chao, D. & Mai, W. Simultaneous regulation on solvation shell and electrode interface for dendrite-free Zn ion batteries achieved by a low-cost glucose additive. *Angew. Chem., Int. Ed.* **60**, 18247-18255, (2021).
27. Huang, C., Zhao, X., Liu, S., Hao, Y., Tang, Q., Hu, A., Liu, Z. & Chen, X. Stabilizing zinc anodes by regulating the electrical double layer with saccharin anions. *Adv Mater* **33**, 2100445, (2021).
28. Xiang, Z. D., Rose, S. & Datta, P. K. Pack deposition of coherent aluminide coatings on γ -TiAl for enhancing its high temperature oxidation resistance. *Surf. Coat. Technol.* **161**, 286-292, (2002).
29. T. P. Moffat, D. Wheeler & Josell, D. Electrodeposition of copper in the SPS-PEG-Cl additive system: I. kinetic measurements: influence of SPS. *J. Electrochem. Soc.* **151**, C262, (2004).

30. Benea, L. & Danaila, E. Nucleation and growth mechanism of Ni/TiO₂ nanoparticles electrocodeposition. *J. Electrochem. Soc.* **163**, D655, (2016).
31. Scharifker, B. & Hills, G. Theoretical and experimental studies of multiple nucleation. *Electrochim. Acta* **28**, 879-889, (1983).
32. Torabi, M. & Dolati, A. A kinetic study on the electrodeposition of nickel nanostructure and its electrocatalytic activity for hydrogen evolution reaction. *J. Appl. Electrochem.* **40**, 1941-1947, (2010).
33. Lu, J. & Barkey, D. P. A thermodynamic study of adsorption of benzyl viologen and polyethylene glycol and their displacement by 3-mercapto-1-propanesulfonate during copper electrodeposition. *J. Electrochem. Soc.* **165**, D231, (2018).
34. Elrouby, M., El -Shafy Shilkamy, H. A. & Elsayed, A. Development of the electrochemical performance of zinc via alloying with indium as anode for alkaline batteries application. *J. Alloys Compd.* **854**, 157285, (2021).
35. Kunsong, M. & Alain, C. P. Colloidal behaviour of montmorillonite in the presence of Fe³⁺ ions. *Colloids Surf., A* **155**, 359-372, (1999).
36. Szilagyi, I., Trefalt, G., Tiraferri, A., Maroni, P. & Borkovec, M. Polyelectrolyte adsorption, interparticle forces, and colloidal aggregation. *Soft Matter* **10**, 2479, (2014).
37. He, P., Yan, M., Zhang, G., Sun, R., Chen, L., An, Q. & Mai, L. Layered VS₂ nanosheet-based aqueous Zn ion battery cathode. *Adv. Energy Mater.* **7**, 1601920, (2017).

Acknowledgments

This research was supported by the National Natural Science Foundation of China (Grant No. 51802225) and the funding from State Key Laboratory of Materials Processing and Die & Mould Technology, Huazhong University of Science and Technology (P2020-001).

Author contributions

R. Z. and L. Q. conceived and designed the research. R. Z. carried out the main experiments. H. W. contributed assistantly the data curation. H. D. helped with the synthesis of VS₂. Y. Y. and Z. G. helped with the Chronoamperogram measurements and analysis. R. Z., L. Q., and Y. H. wrote the manuscript. All authors discussed the results and reviewed the manuscript.

Competing interests

The authors declare no competing interests.

Supplementary Files

This is a list of supplementary files associated with this preprint. Click to download.

- [SupportingInformation.pdf](#)